





27 change; 2) to obtain distributions of minor chemical constituents ( $O_3$ , H, and O) at the  
28 altitudes of the mesopause; and 3) to investigate dynamic processes such as tides, gravity, and  
29 planetary waves (GWs and PWs, respectively), sudden stratospheric warmings (SSWs), and  
30 quasi-biennial oscillation (QBO).

31 Hence, a number of authors have studied temperatures in the mesopause region using airglow  
32 emission ground-based observations focusing on long-term trends (e.g., Bittner et al., 2002;  
33 Holmen et al., 2014; Dalin et al., 2020, and references therein) with attention to seasonal  
34 variations (e.g., Reid et al., 2017, and references therein) and the solar-cycle effect (e.g.,  
35 Kalicinsky et al., 2016, and references therein).

36 Minor chemical constituents as well as chemical heat have also been retrieved by  $OH^*$   
37 emission observations. Ever since atomic oxygen concentration was determined by the rocket-  
38 born detection of  $OH^*$  airglow (Good, 1976), this method has come into wide use for  
39 obtaining information about distributions of minor chemical constituents in the mesopause  
40 region, namely, atomic oxygen concentration (e.g., Russell et al., 2005; Mlynczak et al.,  
41 2013a, and references therein), ozone concentration (e.g., Smith et al., 2009, and references  
42 therein), atomic hydrogen concentration (e.g., Mlynczak et al., 2014, and references therein),  
43 and exothermic chemical heat (e.g., Mlynczak et al., 2013b, and references therein).

44 Numerous works using airglow observations, have been devoted to dynamic processes, for  
45 example, to study mesopause variabilities in time of SSWs (Damiani et al., 2010; Shepherd et  
46 al., 2010). Gao et al. (2011) studied the temporal evolution of nightglow brightness and height  
47 during SSW events. A year earlier, they found a QBO signal in the excited hydroxyl emission  
48 (Gao et al., 2010). The climatology of PWs was investigated in works by Takahashi et al.  
49 (1999), Buriti et al. (2005), and Reisin et al. (2014). Tides were studied by Xu et al. (2010)  
50 and Lopez-Gonzalez et al. (2005). GW parameters based on the airglow technique were  
51 investigated, for example, by Taylor et al. (1991) and Wachter et al. (2015). A more complete



52 description of works in which hydroxyl emissions were used to study dynamic processes can  
53 be found in a review by Shepherd et al. (2012).

54 The morphology of the OH\* layer is an essential component in the interpretation of  
55 observations and in understanding the processes involved in layer variability. Annual  
56 variations in the OH\* layer have been identified at all latitudes (Marsh et al., 2006).  
57 Equatorial and low-latitude semi-annual variations have been observed by satellites (e.g.,  
58 Abreu and Yee, 1989; Liu et al., 2008, and references therein), as well as by ground-based  
59 instruments (Takahashi et al., 1995), and they have been modelled by several research teams  
60 (Le Texier et al., 1987; Marsh et al., 2006, and references therein). The maxima of emissions  
61 were found to occur near equinoxes. In spite of the large number of studies on this subject,  
62 there are still knowledge gaps. Recently, unexpected behaviour in the semi-annual cycle of  
63 excited hydroxyl emission has been found by ground-based observations, with a shift of the  
64 peaks from equinoxes to summer and winter at middle latitudes (Popov et al., 2018; Popov et  
65 al., 2020); this was also found by modelling (Grygalashvyly et al., 2014, Fig. 3). Similar  
66 variations in OH\* emissions with peaks near equinoxes have been observed at middle  
67 latitudes (34.6° N) in the southern hemisphere (Reid et al., 2014). These results were provided  
68 without explanations; in our short paper, we offer a preliminary explanation.

69 The second chapter of our manuscript describes the observational technique and model that  
70 were applied; in the third chapter, we present results and an analysis of observations and  
71 modelling; conclusions are provided in the fourth chapter.

72

## 73 **2. Observational technique and model**

74

### 75 **2.1. Observational technique**

76



77 The spectral airglow temperature imager (SATI), which measures nightglow intensity for  
 78 vibrational transitions of  $\text{OH}^*_{v=6} \rightarrow \text{OH}^*_{v=2}$  and temperature using vibrational-rotational  
 79 transitions, was assembled at the Institute of Ionosphere ( $43^\circ$  N,  $77^\circ$  E) in Almaty,  
 80 Kazakhstan. It represents a Fabry-Perot spectrometer with a CCD (charge-coupled device)  
 81 camera as a detector and a narrow-band interference filter as the etalon. Following Lopez-  
 82 Gonzalez et al. (2007), we use an interference filter with the centre at 836.813 nm and a  
 83 bandwidth of 0.182 nm. This corresponds to the spectral region of the  $\text{OH}^*(6-2)$  band. In  
 84 order to infer the temperature, the calculated spectra for different vibro-rotational transitions  
 85 are compared with those from observations. The SATI operates at a sixty-second exposure  
 86 that provides corresponding time resolution. The method of temperature retrieval is well-  
 87 described by Lopez-Gonzalez et al. (2004). The observations of temperature were validated  
 88 using satellite SABER measurements (Lopez-Gonzalez et al., 2007; Pertsev et al., 2013).  
 89 Additional details about this instrument are presented in many papers (Wies et al., 1997;  
 90 Aushev et al., 2000; Lopez-Gonzalez et al., 2004, 2005, 2007, 2009).

91

## 92 2.2. Model and numerical experiment

93

94 The model of excited hydroxyl (MEH) calculates the  $\text{OH}^*$  number densities at each  
 95 vibrational level  $v$  as the production divided by losses (excited hydroxyl is assumed in the  
 96 photochemical equilibrium), which include the chemical sources as well as collisional and  
 97 emissive removal:

$$98 \quad [\text{OH}_v] = \frac{\left( \zeta_v a_1 [\text{O}_3][\text{H}] + \psi_v a_2 [\text{O}][\text{HO}_2] + \sum_{v'=v+1}^9 B_{v'v} [\text{O}_2][\text{OH}_{v'}] + C_{v+1} [\text{N}_2][\text{OH}_{v+1}] + \right.}{\left( a_3(v)[\text{O}] + \sum_{v''=0}^{v-1} D_{vv''} [\text{O}] + C_v [\text{N}_2] + \right.} \left. \frac{\left. + \sum_{v'=v+1}^9 D_{v'v} [\text{O}][\text{OH}_{v'}] + \sum_{v'=v+1}^9 E_{v'v} [\text{OH}_{v'}] \right)}{\left. + \sum_{v''=0}^{v-1} B_{vv''} [\text{O}_2] + \sum_{v''=0}^{v-1} E_{vv''} \right)}, \quad \left( \begin{matrix} v < v' \\ v'' < v \end{matrix} \right). \quad (1)$$

99 The first term in the numerator of (1) is the reaction  $\text{O}_3 + \text{H} \rightarrow \text{OH}_v + \text{O}$ , where  $a_1$  is the  
 100 reaction rate, and  $\zeta_v$  represents the branching ratios (Adler-Golden, 1997). The second term is



101 the  $O + HO_2 \rightarrow OH_v + O_2$  reaction, where  $a_2$  and  $\psi_v$  are the reaction rate and nascent  
102 distribution, respectively (Kaye (1988) after Takahashi and Batista (1981)). The other three  
103 summands represent the populations resulting from collisional relaxation from higher  $v$ -  
104 levels, where  $B$ ,  $C$ , and  $D$  are the collisional deactivation coefficients for  $O_2$  (Adler-Golden,  
105 1997),  $N_2$  (Makhlouf et al., 1995), and  $O$  (Caridade et al., 2013), respectively. The last  
106 summand is the multi-quantum population by spontaneous emissions, where  $E_{vv}$  is the  
107 spontaneous emission coefficient (Xu et al., 2012). The losses occur, additionally, through the  
108 chemical removal of the excited hydroxyl by atomic oxygen, where  $a_3(v)$  is the vibrationally  
109 dependent reaction rate (Varandas et al., 2004). The calculations in Eq. (1) are incorporated  
110 into the chemistry-transport model (CTM).

111 Here, we enumerate only the main features of the CTM as one can find extended descriptions  
112 in manyworks (Sonnemann and Grygalashvyly, 2020; Grygalashvyly et al., 2014; and  
113 references therein). The CTM consists of four blocks: chemical, transport, radiative, and  
114 diffusive. The chemical block accounts for 19 constituents, and 63 photo-dissociations and  
115 chemical reactions (Burkholder et al., 2015). The chemical code utilises a family approach  
116 with the odd-oxygen ( $O(^1D)$ ,  $O$ ,  $O_3$ ), odd-hydrogen ( $H$ ,  $OH$ ,  $HO_2$ ,  $H_2O_2$ ), and odd-nitrogen  
117 ( $N(^2D)$ ,  $N(^4S)$ ,  $NO$ ,  $NO_2$ ) families (Shimazaki, 1985). In the radiative part, the dissociation  
118 rates are taken from a pre-calculated table depending on zenith angle and altitude (Kremp et  
119 al., 1999). The transport block calculates advections in three directions following Walcek  
120 (2000). The diffusive part accounts for only vertical molecular plus turbulent diffusion  
121 (Morton and Mayers, 1994). This model has been validated against observations of ozone,  
122 which plays a role in the formation of  $OH^*$  (e.g., Hartogh et al., 2011; Sonnemann et al.,  
123 2007; and references therein) and water vapour, which is the principal source of odd-  
124 hydrogens and, particularly, of atomic hydrogen (e.g., Hartogh et al., 2010; Sonnemann et al.,  
125 2008; and references therein). Our current analysis used the run for year 2009, which was



126 published and described in a number of works (Grygalashvyly et al., 2014, section 4;  
127 Sonnemann et al., 2015).

128 Here we assume that the structures in the longitudinal direction are equivalent to local time  
129 (LT) behaviour, with 24 LT related to midnight at 0° longitude. The LTs of successive  
130 longitudes are used to analyse our calculations. Hence, in the following figures related to the  
131 model results, longitude is used as the so-called ‘pseudo time’. The night-time averaged  
132 values account for the period from 21:45 LT to 2:15 LT. For the purposes of our discussion,  
133 we use ‘pressure-altitude’ (or other words ‘pseudo-altitude’)  $Z^* = -H \ln(P/P_0)$ , where  $P$   
134 represents pressure:  $P_0 = 1013 \text{ mbar}$  is the surface pressure, and  $H = 7 \text{ km}$  is the scale  
135 height.

136

### 137 3. Results and discussion

138

139 Figure 1a illustrates the nightly mean monthly averaged values of the observed annual  
140 variability of intensity at 43° N (red line) and the modelled annual variability of volume  
141 emission at the peak of the OH\* layer at 43.75° N (black line), both for transition  
142  $\text{OH}^*_{v=6} \rightarrow \text{OH}^*_{v=2}$ . The error bar shows standard deviation. By the observations as well as by  
143 modelling, we can clearly see semi-annual variations of emissions with peaks in winter and  
144 summer.

145 Grygalashvyly et al. (2014), Sonnemann et al. (2015), and Grygalashvyly (2015) have derived  
146 and confirmed through modelling that the concentration of excited hydroxyl (hence, volume  
147 emission and intensity) at peak is directly proportional to the product of the surrounding  
148 pressure (hence, it depends on altitude), atomic oxygen number density, and the negative  
149 power of temperature (Eq. A2 in the Appendix). Thus, in order to infer the reasons for this  
150 semi-annual variation, one should consider three drivers of OH\* variability: temperature,  
151 atomic oxygen concentration, and height of the layer.



152 Figure 1b shows the monthly mean nightly averaged values of the observed annual variability  
153 of temperature at 43° N (red line) and the modelled annual variability of temperature at the  
154  $OH_{v=6}^*$  peak at 43.75° N (black line). Both the observations and the modelling show minima  
155 in summer and maxima in winter. Hence, the temperature decline can be one of the reasons  
156 for the summer intensity (and volume emission) peak.

157 Figures 1c and 1d depict modelled monthly mean nightly averaged values of atomic oxygen at  
158  $OH_{v=6}^*$  peak and the height of the excited hydroxyl peak, respectively, at 43.75° N. The  
159 modelling shows the peaks of atomic oxygen concentration in July and December–January,  
160 with the largest values in winter. The variation of height through the year occurs from ~90 km  
161 to 94 km. This is an essential variability and provides input to the variability of the  
162 concentration of the surrounding air.

163 In order to study the morphology of this semi-annual variation and assess the impacts of  
164 temperature, atomic oxygen concentration, and height (concentration of air) variability, we  
165 calculate one-month sliding averaged values based on the model results. Figure 2 illustrates  
166 the modelled annual variability at the  $OH_{v=6}^*$  peak: a) volume emission ( $OH_{v=6}^* \rightarrow OH_{v=2}^*$ ), b)  
167 temperature, c) atomic oxygen concentration, and d) height.

168 The summer maximum of volume emission (Fig. 2a) shows the strongest values in July and is  
169 extended from ~30° N to ~50° N. The summer maximum is stronger than that in winter. The  
170 winter maximum has its strongest values in January and a positive gradient into the winter  
171 pole direction; at latitudes 30°–50° N, it represents the rest of the annual variation at high  
172 latitudes that occurs because of the annual variation in general mean circulation and fluxes of  
173 atomic oxygen which correspond to this variability (Liu et al., 2008; Marsh et al., 2006).

174 Similar behaviour of the emissions for transition  $OH_{v=8}^* \rightarrow OH_{v=3}^*$  was captured by WINDII  
175 (Wind Imaging Interferometer) and modelled by Thermosphere-Ionosphere-Mesosphere  
176 Electrodynamics General Circulation Model at 84–88 km (Liu et al., 2008, Fig. 5 and 6).



177 The temperature (Fig. 2b) shows a clear annual variation from the middle to the high  
178 latitudes, with a minimum  $\sim 150$  K at middle latitudes in July. The summer minimum at the  
179 middle latitudes is an echo of those at high latitudes. The atomic oxygen concentrations (Fig.  
180 2c) reveal the annual cycle. The concentrations have a maximum in winter and a minimum in  
181 summer at high and middle latitudes, as has already been observed (Smith et al., 2010).  
182 However, in the region from  $\sim 30^\circ$  to  $\sim 50^\circ$  N in summer, atomic oxygen concentrations show  
183 one additional peak in June–July. Formation of this summer peak can be explained by the  
184 transformed Eulerian mean (TEM) circulation (Limpasuvan et al., 2012, Fig. 7; Limpasuvan  
185 et al., 2016, Fig. 5), which brings into the summer hemisphere the air reached by atomic  
186 oxygen from the region of its production at high latitudes above 100 km to  $\sim 90$  km at  $\sim 30^\circ$ –  
187  $50^\circ$  N. The peak altitude of the  $OH_{v=6}^*$  (Fig. 2d) shows complex annual variability. There is a  
188 secondary maximum  $OH^*$  peak at  $\sim 30^\circ$ – $50^\circ$  N in summer.

189 In order to assess the input into annual variability from different sources, we calculate relative  
190 to annual averaged variations of volume emissions due to atomic oxygen, temperature, and air  
191 density (Eq. A6). The derivation of these parameters is presented in the appendix. A similar  
192 approach can be useful for analysing emission variations due to GWs, PWs, and tides.

193 Figure 3a shows relative variations of emissions due to impacts of atomic oxygen (black line),  
194 temperature (red line), and air density (green line) at  $43.75^\circ$  N. The strongest emission  
195 variation occurs because of changes in atomic oxygen concentration: the amplitude of its  
196 relative deviation amounts to  $\sim 50\%$ . The amplitudes of relative deviations of emissions due to  
197 temperature and air density amount to  $\sim 15\%$  and  $\sim 20\%$ , respectively. The atomic oxygen  
198 variation gives the most essential input into the winter maximum of emission (black line).  
199 Because of the downward transport of atomic oxygen in winter, the volume emission rises by  
200  $\sim 50\%$  averaged annually. The summer maximum is determined by the superposition of all  
201 three factors. After the spring reduction of emissions due to the decline of atomic oxygen  
202 concentration ( $\sim 40\%$  of annual averaged values), the emissions rise again to approximately



203 the annual average values in June–July. This is synchronised with the growth of volume  
204 emissions by ~20% over the annual average values due to summer temperature declines (red  
205 line) and with the growth of volume emissions by ~15% over the annual average due to the  
206 decline of peak altitude in April–September and the corresponding rise of air density (green  
207 line).

208 Figure 3b illustrates relative variations of emissions due to second momenta (Eq. A7 in the  
209 Appendix). The second momenta do not provide essential input to annual variation. The  
210 strongest among them,  $\frac{[O]M'}{[O]M}$  (blue line), gives emission variability with an amplitude ~6% of  
211 annual averaged values.

212 In the context of our short paper, the ultimate question regarding the role of tides and GWs on  
213 semi-annual variations of OH\* emissions at middle latitudes has not been answered.  
214 Undoubtedly, the simultaneous analysis of observations of excited hydroxyl emissions from  
215 several stations is desirable to explore this question.

216

#### 217 **4. Summary and conclusions**

218

219 Based on observations and numerical simulation, we confirmed the existence of a  
220 semi-annual cycle of excited hydroxyl emission at middle latitudes with maxima in summer  
221 (June–July) and winter (December–January). The annual variation in general mean circulation  
222 and atomic oxygen concentration corresponding to the excited hydroxyl emission cycle was  
223 found to be the leading cause of the winter maximum of this cycle, whereas the summer  
224 maximum represents the superposition of three different processes: atomic oxygen meridional  
225 transport due to residual circulation from the summer pole to the equator; temperature decline,  
226 which represents the rest of the mesopause cooling at summer high latitudes; and air



227 concentration growth at the peak of the excited hydroxyl emission layer due to hydroxyl layer  
228 descent at middle latitudes in April–September.

229

### 230 **Appendix.**

231

232 To obtain the derivation, we start with a simplified equation for excited hydroxyl  
233 concentration. Taking into account that the ozone is in photochemical equilibrium in the  
234 vicinity of the  $[OH_v]$  layer and above during night-time (Kulikov et al., 2018; Belikovich et  
235 al., 2018; Kulikov et al., 2019); utilising the equation for ozone balance during night-time  
236 ( $a_5[O_3][O] + a_1[H][O_3] = a_4[O][O_2][M]$ ), where  $a_4$  and  $a_5$  are the coefficients for the  
237 corresponding reactions; omitting the reaction of atomic oxygen with ozone as relatively slow  
238 (Smith et al., 2008); substituting the reduced ozone balance equation for the excited hydroxyl  
239 balance equation (first term in the numerator of Eq. (1)); assuming that the most effective  
240 production of excited hydroxyl occurs due to the reaction of ozone with atomic hydrogen and  
241 that the most effective losses are due to quenching with molecular oxygen; we obtain from  
242 Eq. (1) a simplified expression in which excited hydroxyl concentration is represented in  
243 terms of atomic oxygen concentration, temperature (in  $a_4$ ), and concentration of the  
244 surrounding air:

$$245 \quad [OH_v] \approx \mu_v a_4 [O][M]. \quad (A1)$$

246 Here  $\mu_v = \frac{\zeta_v + \sum_{v'=v+1}^{v'=9} \mu_{v'} B_{v'v}}{\sum_{v''=0}^{v''=v-1} B_{vv''}}$ , ( $\zeta_{v>9} = 0$ ) are the coefficients representing the arithmetic

247 combination of branching ratios  $\zeta_v$  and quenching coefficients  $B_{v'v}$ . More comprehensive  
248 derivations of (A1) can be found in a number of papers (Grygalashvyly et al., 2014;  
249 Grygalashvyly, 2015; Grygalashvyly and Sonnemann, 2020). Although this is too simplified  
250 to be used for precise calculations, it is useful for obtaining information about impacts and for  
251 assessing variabilities.



252 By multiplying (A1) by the Einstein-coefficient  $E_{vv''}$  for given a transition, writing the  
 253 reaction rate explicitly  $a_4 = 6 \cdot 10^{-34} (300/T)^{2.4}$  (Burkholder et al., 2015), and collecting all  
 254 constants in  $\chi_{vv''}$ , we obtain an expression for volume emission in terms of atomic oxygen  
 255 concentration, temperature, and air number density:

$$256 \quad V \approx \chi_{vv''} T^{-2.4} [O][M], \quad (A2)$$

257 where  $\chi_{vv''} = \mu_v E_{vv''} \cdot 6 \cdot 10^{-34} \cdot 300^{2.4}$ .

258 Next, we apply Reynolds decomposition by averaged and variable part to the temperature,  
 259 atomic oxygen concentration, and concentration of air in (A2):

$$260 \quad V \approx \chi_{vv''} (\bar{T} + T')^{-2.4} (\bar{[O]} + [O]') (\bar{[M]} + [M]'), \quad (A3)$$

261 where  $\bar{T}$ ,  $\bar{[O]}$ ,  $\bar{[M]}$  are average parts, and  $T'$ ,  $[O]'$ ,  $[M]'$  are the corresponding varying parts.

262 After decomposing the term with temperature in the Taylor expansion and cross-multiplying  
 263 all terms of (A3), we obtain:

$$264 \quad V \approx \chi_{vv''} \bar{T}^{-2.4} \bar{[O]} \cdot \bar{[M]} + \chi_{vv''} \bar{T}^{-2.4} \bar{[O]} [M]' + \chi_{vv''} \bar{T}^{-2.4} [O]' \bar{[M]} - 2.4 \chi_{vv''} T' \bar{T}^{-3.4} \bar{[O]} \cdot$$

$$265 \quad \bar{[M]} + \chi_{vv''} \bar{T}^{-2.4} [O]' [M]' - 2.4 \chi_{vv''} T' \bar{T}^{-3.4} \bar{[O]} [M]' - 2.4 \chi_{vv''} T' \bar{T}^{-3.4} [O]' \bar{[M]} -$$

$$266 \quad 2.4 \chi_{vv''} T' \bar{T}^{-3.4} [O]' [M]'. \quad (A4)$$

267 The volume emission for a given transition can be represented as follows:

$$268 \quad V \approx \bar{V} + V'_M + V'_O + V'_T + V''_{OM} + V''_{TM} + V''_{TO} + \text{higher momenta}, \quad (A5)$$

269 where,  $\bar{V} = \chi_{vv''} \bar{T}^{-2.4} \bar{[O]} \cdot \bar{[M]}$ ,  $V'_M = \chi_{vv''} \bar{T}^{-2.4} \bar{[O]} [M]'$ ,  $V'_O = \chi_{vv''} \bar{T}^{-2.4} [O]' \bar{[M]}$ ,  $V'_T =$   
 270  $-2.4 \chi_{vv''} T' \bar{T}^{-3.4} \bar{[O]} \cdot \bar{[M]}$ ,  $V''_{OM} = \chi_{vv''} \bar{T}^{-2.4} [O]' [M]'$ ,  $V''_{TM} =$   
 271  $-2.4 \chi_{vv''} T' \bar{T}^{-3.4} \bar{[O]} [M]'$ ,  $V''_{TO} = -2.4 \chi_{vv''} T' \bar{T}^{-3.4} [O]' \bar{[M]}$ .

272 Hence, relative deviations (RD) of emissions due to variations in atomic oxygen, temperature,  
 273 and concentration of air are:



$$\begin{aligned} RD'_O &= 100\% \cdot \frac{V'_O}{\bar{V}} = 100\% \cdot \frac{[O]'}{[O]}, \\ 274 \quad RD'_T &= 100\% \cdot \frac{V'_T}{\bar{V}} = 100\% \cdot -2.4 \frac{T'}{\bar{T}}, \\ RD'_M &= 100\% \cdot \frac{V'_M}{\bar{V}} = 100\% \cdot \frac{[M]'}{[M]}. \end{aligned} \quad (A6)$$

275 The relative deviations (RD) of emissions due to second momenta are

$$\begin{aligned} RD''_{OM} &= 100\% \cdot \frac{V''_{OM}}{\bar{V}} = 100\% \cdot \frac{[O]'[M]'}{[O][M]}, \\ 276 \quad RD''_{TM} &= 100\% \cdot \frac{V''_{TM}}{\bar{V}} = 100\% \cdot -2.4 \frac{T'[M]'}{\bar{T}[M]}, \\ RD''_{TO} &= 100\% \cdot \frac{V''_{TO}}{\bar{V}} = 100\% \cdot -2.4 \frac{T'[O]'}{\bar{T}[O]}. \end{aligned} \quad (A7)$$

277

278 **Data availability.** The data utilized in this manuscript can be downloaded from  
279 [http://ra.rshu.ru/files/Grygalashvyly\\_et\\_al\\_ANGEO\\_2020](http://ra.rshu.ru/files/Grygalashvyly_et_al_ANGEO_2020).

280 **Author contributions.** All authors contributed equally to this paper.

281 **Competing interests.** The authors declare that they have no conflict of interest.

282 **Acknowledgements.** This work was supported by the Russian Science Foundation (grant  
283 #20-77-10006). Some data processing have been done under the state task of the Ministry of  
284 science and higher education of the Russian Federation (project FSZU-2020-0009)".

285

## 286 References

287

288 Abreu, V. J., and Yee, J. H.: Diurnal and seasonal variation of the nighttime OH (8-3)  
289 emission at low latitudes, J. Geophys. Res., 94(A9), 11949-11957, doi:10.1029/89JA00619,  
290 1989.

291



292 Adler-Golden, S.: Kinetic parameters for OH nightglow modeling consistent with recent  
293 laboratory measurements, *J. Geophys. Res.*, 102(A9), 19969–19976, doi:10.1029/97JA01622,  
294 1997.

295

296 Aushev, V. M., Pogoreltsev, A. I., Vodyannikov, V. V., Wiens, R. H., and Shepherd, G. G.:  
297 Results of the airglow and temperature observations by MORTI at the Almaty site (43.05 N,  
298 76.97 E), *Phys. Chem. Earth*, 25(5–6), 409–415, doi:10.1016/S1464-1909(00)00035-6, 2000.

299

300 Belikovich, M. V., Kulikov, M. Yu., Grygalashvyly, M., Sonnemann, G. R., Ermakova, T. S.,  
301 Nechaev, A. A., and Feigin, A. M.: Ozone chemical equilibrium in the extended mesopause  
302 under the nighttime conditions. *Adv. Space Res.*, 61, 426–432, doi: 10.1016/j.asr.2017.10.010,  
303 2018.

304

305 Bittner, M., Offermann, D., Graef, H.-H., Donner, M., and Hamilton, K.: An 18 year time  
306 series of OH rotational temperatures and middle atmosphere decadal variations, *J. Atmos. Sol.*  
307 *Terr. Phys.*, 64, 1147–1166, doi:10.1016/S1364-6826(02)00065-2, 2002.

308

309 Buriti, R. A., Takahashi, H., Lima, L. M., and Medeiros, A. F.: Equatorial planetary waves in  
310 the mesosphere observed by airglow periodic oscillations, *Adv. Space Res.*, 35, 2031–2036,  
311 doi: 10.1016/j.asr.2005.07.012, 2005.

312

313 Burkholder, J. B., Sander, S. P., Abbatt, J., Barker, J. R., Huie, R. E., Kolb, C. E., Kurylo, M.  
314 J., Orkin, V. L., Wilmouth, D. M., and Wine, P. H.: Chemical Kinetics and Photochemical  
315 Data for Use in Atmospheric Studies, Evaluation No. 18, JPL Publication 15-10, Jet  
316 Propulsion Laboratory, Pasadena, <http://jpldataeval.jpl.nasa.gov>, 2015.

317



318 Caridade, P. J. S. B., Horta, J.-Z. J., and Varandas, A. J. C.: Implications of the O + OH  
319 reaction in hydroxyl nightglow modeling, *Atmos. Chem. Phys.*, 13, 1-13, doi:10.5194/acp-13-  
320 1-2013, 2013.

321

322 Dalin, P., Perminov, V., Pertsev, N., and Romejko, V.: Updated long-term trends in  
323 mesopause temperature, airglow emissions, and noctilucent clouds, *J. Geophys. Res. Atmos.*,  
324 125, e2019JD030814, doi.org/10.1029/2019JD030814, 2020.

325

326 Damiani, A., Storini, M., Santee, M. L., and Wang, S.: Variability of the nighttime OH layer  
327 and mesospheric ozone at high latitudes during northern winter: influence of meteorology,  
328 *Atmos. Chem. Phys.*, 10, 10291-10303, doi:10.5194/acp-10-10291-2010, 2010.

329

330 Gao, H., Xu, J., and Wu, Q.: Seasonal and QBO variations in the OH nightglow emission  
331 observed by TIMED/SABER, *J. Geophys. Res.*, 115, A06313, doi:10.1029/2009JA014641,  
332 2010.

333

334 Gao, H., Xu, J., Ward, W., and Smith, A. K.: Temporal evolution of nightglow emission  
335 responses to SSW events observed by TIMED/SABER, *J. Geophys. Res.*, 116, D19110,  
336 doi:10.1029/2011JD015936, 2011.

337

338 Garcia, R. R., and Solomon, S.: The effect of breaking gravity waves on the dynamics and  
339 chemical composition of the mesosphere and lower thermosphere, *J. Geophys. Res.*, 90(D2),  
340 3850–3868, doi:10.1029/JD090iD02p03850, 1985.

341

342 Good, R. E.: Determination of atomic oxygen density from rocket borne measurements of  
343 hydroxyl airglow, *Planet. Space Sci.*, 24, 389–395, doi:10.1016/0032-0633(76)90052-0, 1976.



344

345 Grygalashvyly, M., Sonnemann, G. R., Lübken, F.-J., Hartogh, P., and Berger, U.: Hydroxyl  
346 layer: Mean state and trends at midlatitudes, *J. Geophys. Res.*, 119, 12391–12419,  
347 doi:10.1002/2014JD022094, 2014.

348

349 Grygalashvyly, M.: Several notes on the OH\*-layer, *Ann. Geophys.*, 33, 923-930,  
350 doi:10.5194/angeo-33-923-2015, 2015.

351

352 Grygalashvyly, M., and Sonnemann, G. R.: Note on Consistency between Kalogerakis-  
353 Sharma Mechanism (KSM) and Two-Step Mechanism of Atmospheric Band Emission, *Earth*  
354 *Planets Space*, accepted, 2020.

355

356 Hartogh, P., Sonnemann, G. R., Grygalashvyly, M., Li, S., Berger, U., and Lübken, F.-J.:  
357 Water vapor measurements at ALOMAR over a solar cycle compared with model calculations  
358 by LIMA, *J. Geophys. Res.*, 114, doi:10.1029/2009JD012364, 2010.

359

360 Hartogh, P., Jarchow, C., Sonnemann, G. R., and Grygalashvyly, M.: Ozone distribution in  
361 the middle latitude mesosphere as derived from microwave measurements at Lindau (51.66°  
362 N, 10.13° E), *J. Geophys. Res.*, 116, D04305, doi:10.1029/2010JD014393, 2011.

363

364 Holmen, S. E., Dyrland, M. E., and Sigernes, F.: Long-term trends and the effect of solar  
365 cycle variations on mesospheric winter temperatures over Longyearbyen, Svalbard (78°N), *J.*  
366 *Geophys. Res. Atmos.*, 119, 6596–6608, doi:10.1002/2013JD021195, 2014.

367



368 Kalicinsky, C., Knieling, P., Koppmann, R., Offermann, D., Steinbrecht, W., and Wintel, J.:  
369 Long-term dynamics of OH\* temperatures over central Europe: trends and solar correlations,  
370 Atmos. Chem. Phys., 16, 15033-15047, doi:10.5194/acp-16-15033-2016, 2016.

371

372 Kaye, J. A.: On the possible role of the reaction  $O + HO_2 \rightarrow OH + O_2$  in OH airglow, J.  
373 Geophys. Res., 93, 285–288, doi:10.1029/JA093iA01p00285, 1988.

374

375 Kremp, Ch., Berger, U., Hoffmann, P., Keuer, D., and Sonnemann, G. R.: Seasonal variation  
376 of middle latitude wind fields of the mesopause region -a comparison between observation  
377 and model calculation, Geophys. Res. Lett., 26, 1279-1282, doi:10.1029/1999GL900218,  
378 1999.

379

380 Kulikov, M. Yu., Belikovich, M. V., Grygalashvyly, M., Sonnemann, G. R., Ermakova, T. S.,  
381 Nechaev, A. A., and Feigin, A. M.: Nighttime ozone chemical equilibrium in the mesopause  
382 region, J. Geophys. Res., 123, 3228-3242, doi: 10.1002/2017JD026717, 2018.

383

384 Kulikov, M. Yu., Nechaev, A. A. , Belikovich, M. V., Vorobeva, E. V., Grygalashvyly, M.,  
385 Sonnemann, G. R., and Feigin, A. M.: Boundary of Nighttime Ozone Chemical Equilibrium  
386 in the Mesopause Region from SABER Data: Implications for Derivation of Atomic Oxygen  
387 and Atomic Hydrogen, Geophys. Res. Lett., 46, 997-1004, doi:10.1029/2018GL080364,  
388 2019.

389

390 Le Texier, H., Solomon, S., and Garcia, R. R.: Seasonal variability of the OH Meinel bands,  
391 Planet. Space Sci., 35(8), 977-989, doi:10.1016/0032-0633(87)90002-X, 1987.

392



393 Limpasuvan, V., Richter, J. H., Orsolini, Y. J., Stordal, F., and Kvissel, O.-K.: The roles of  
394 planetary and gravity waves during a major stratospheric sudden warming as characterized by  
395 WACCM, *J. Atmos. Sol. Terr. Phys.*, 78–79, 84–98, doi:10.1016/j.jastp.2011.03.004, 2012.

396

397 Limpasuvan, V., Orsolini, Y. J., Chandran, A., Garcia, R. R., and Smith, A. K.: On the  
398 composite response of the MLT to major sudden stratospheric warming events with elevated  
399 stratopause, *J. Geophys. Res. Atmos.*, 121, 4518–4537, doi:10.1002/2015JD024401, 2016.

400

401 Liu, G., and Shepherd, G. G.: An empirical model for the altitude of the OH nightglow  
402 emission, *Geophys. Res. Lett.*, 33, L09805, doi:10.1029/2005GL025297, 2006.

403

404 Liu, G., Shepherd, G. G., and Roble, R. G.: Seasonal variations of the nighttime O(<sup>1</sup>S) and  
405 OH airglow emission rates at mid-to-high latitudes in the context of the large-scale  
406 circulation, *J. Geophys. Res.*, 113, A06302, doi:10.1029/2007JA012854, 2008.

407

408 Lopez-Gonzalez, M. J., Rodriguez, E., Wiens, R. H., Shepherd, G. G., Sargoytchev, S.,  
409 Brown, S., Shepherd, M. G., Aushev, V. M., Lopez-Moreno, J. J., Rodrigo, R., and Cho, Y.-  
410 M.: Seasonal variations of O<sub>2</sub> atmospheric and OH(6–2) airglow and temperature at mid-  
411 latitudes from SATI observations, *Ann. Geophys.*, 22, 819–828, doi: 10.5194/angeo-22-819-  
412 2004, 2004.

413

414 Lopez-Gonzalez, M. J., Rodriguez, E., Shepherd, G. G., Sargoytchev, S., Shepherd, M. G.,  
415 Aushev, V. M., Brown, S., Garcia-Comas, M., and Wiens, R. H.: Tidal variations of O<sub>2</sub>  
416 Atmospheric and OH(6–2) airglow and temperature at mid-latitudes from SATI observations,  
417 *Ann. Geophys.*, 23, 3579–3590, doi:10.5194/angeo-23-3579-2005, 2005.

418



419 Lopez-Gonzalez, M. J., Garcia-Comas, M., Rodriguez, E., Lopez-Puertas, M., Shepherd, M.  
420 G., Shepherd, G. G., Sargoytchev, S., Aushev, V. M., Smith, S. M., Mlynczak, M. G.,  
421 Russell, J. M., Brown, S., Cho, Y.-M., and Wiens, R. H.: Ground-based mesospheric  
422 temperatures at mid-latitude derived from O<sub>2</sub> and OH (6-2) airglow SATI data: Comparison  
423 with SABER measurements, *J. Atmos. Solar-Terr. Phys.*, 69, 2379–2390.  
424 doi:10.1016/j.jastp.2007.07.004, 2007.

425

426 Lopez-Gonzalez, M. J., Rodríguez, E., Garcia-Comas, M., Costa, V., Shepherd, M. G.,  
427 Shepherd, G. G., Aushev, V. M., and Sargoytchev, S.: Climatology of planetary wave type  
428 oscillations with periods of 2–20 days derived from O<sub>2</sub> atmospheric and OH(6-2) airglow  
429 observations at mid-latitude with SATI, *Ann.Geophys.*, 27, 3645–3662, doi:10.5194/angeo-  
430 27-3645-2009, 2009.

431

432 Makhlof, U. B., Picard, R. H., and Winick, J. R.: Photochemical-dynamical modeling of the  
433 measured response of airglow to gravity waves. 1. Basic model for OH airglow, *J. Geophys.*  
434 *Res.*, 100, 11289–11311, doi:10.1029/94JD03327, 1995.

435

436 Marsh, D. R., Smith, A. K., Mlynczak, M. G., and Russell III, J. M.: SABER observations of  
437 the OH Meinel airglow variability near the mesopause, *J. Geophys. Res.*, 111, A10S05,  
438 doi:10.1029/2005JA011451, 2006.

439

440 Mlynczak, M. G., Hunt, L. A., Mast, J. C., Marshall, B. T., Russell III, J. M., Smith, A. K.,  
441 Siskind, D. E., Yee, J.-H., Mertens, C. J., Martin-Torres, F. J., Thompson, R. E., Drob, D. P.,  
442 and Gordley, L. L.: Atomic oxygen in the mesosphere and lower thermosphere derived from  
443 SABER: Algorithm theoretical basis and measurement uncertainty, *J. Geophys. Res. Atmos.*,  
444 118, 5724–5735, doi:10.1002/jgrd.50401, 2013a.



445

446 Mlynczak, M. G., Hunt, L. A., Mertens, C. J., Marshall, B. T., Russell III, J. M., Lopez-  
447 Puertas, M., Smith, A. K., Siskind, D. E., Mast, J. C., Thompson, R. E., and Gordley, L. L.:  
448 Radiative and energetic constraints on the global annual mean atomic oxygen concentration in  
449 the mesopause region, *J. Geophys. Res. Atmos.*, 118, 5796–5802, doi:10.1002/jgrd.50400,  
450 2013b.

451

452 Mlynczak, M. G., Hunt, L. A., Marshall, B. T., Mertens, C. J., Marsh, D. R., Smith, A. K.,  
453 Russell, J. M., Siskind, D. E., and Gordley, L. L.: Atomic hydrogen in the mesopause region  
454 derived from SABER: Algorithm theoretical basis, measurement uncertainty, and results, *J.*  
455 *Geophys. Res.*, 119, 3516–3526, doi:10.1002/2013JD021263, 2014.

456

457 Morton, K. W., and D. F. Mayers, D. F.: *Numerical Solution of Partial Differential Equations*,  
458 Cambridge University Press, 1994.

459

460 Pertsev N. N., Andreyev A. B., Merzlyakov E. G., and Perminov V. I.: Mesosphere-  
461 thermosphere manifestations of strato-spheric warmings: joint use of satellite and ground-  
462 based measurements, *Current Problems in Remote Sensing of the Earth from Space*, 10(1),  
463 93–100, <http://jr.rse.cosmos.ru/article.aspx?id=1154&lang=eng>, 2013.

464

465 Popov, A. A., Gavrilov, N. M., Andreev, A. B., and Pogoreltsev, A. I.: Interannual dynamics  
466 in intensity of mesoscale hydroxyl nightglow variations over Almaty, *Solar-Terr. Phys.*, 4(2),  
467 63–68, doi:10.12737/stp-42201810, 2018.

468

469 Popov, A. A., Gavrilov, N. M., Perminov, V. I., Pertsev, N. N., and Medvedeva, I. V.: Multi-  
470 year observations of mesoscale variances of hydroxyl nightglow near the mesopause at Tory



471 and Zvenigorod, J. Atmos. Solar-Terr. Phys., 205, 1-8, doi:10.1016/j.jastp.2020.105311,  
472 2020.

473

474 Reid, I. M., Spargo, A. J., and Woithe, J. M.: Seasonal variations of the nighttime O(<sup>1</sup>S) and  
475 OH (8-3) airglow intensity at Adelaide, Australia, J. Geophys. Res. Atmos., 119, 6991–7013,  
476 doi:10.1002/2013JD020906, 2014.

477

478 Reid, I. M., Spargo, A. J., Woithe, J. M., Klekociuk, A. R., Younger, J. P., and G. G. Sivjee,  
479 G. G.: Seasonal MLT-region nightglow intensities, temperatures, and emission heights at a  
480 Southern Hemisphere midlatitude site, Ann. Geophys., 35, 567-582, doi:10.5194/angeo-35-  
481 567-2017, 2017.

482

483 Reisin, E., Scheer, J., Dyrland, M. E., Sigernes, F., Deehr, C. S., Schmidt, C., Höppner, K.,  
484 Bittner, M., Ammosov, P. P., Gavrilyeva, G. A., Stegman, J., Perminov, V. I., Semenov, A. I.,  
485 Knlieling, P., Koomann, R., Shiokawa, K., Lowe, R. P., Lopez-Gonzalez, M. J., Rodriguez,  
486 E., Zhao, Y., Taylor, M. J., Buriti, R. A., Espy, P. E., French, W. J., Eichmann, K.-U.,  
487 Burrows, J. P., and von Savigny, C.: Traveling planetary wave activity from mesopause  
488 region airglow temperatures determined by the Network for the Detection of Mesospheric  
489 Change (NDMC), J. Atmos. Sol.-Terr. Phys., 119, 71–82, doi:10.1016/j.jastp.2014.07.002,  
490 2014.

491

492 Russell, J. P., Ward, W. E., Lowe, R. P., Roble, R. G., Shepherd, G. G., and B. Solheim, B.:  
493 Atomic oxygen profiles (80 to 115 km) derived from Wind Imaging Interferometer/Upper  
494 Atmospheric Research Satellite measurements of the hydroxyl and greenline airglow: Local  
495 time–latitude dependence, J. Geophys. Res., 110, D15305, doi:10.1029/2004JD005570, 2005.

496



497 Shepherd, G. G., Thuillier, G., Cho, Y.-M., Duboin, M.-L., Evans, W. F. J., Gault, W. A.,  
498 Hersom, C., Kendall, D. J. W., Lathuillère, C., Lowe, R. P., McDade, I. C., Rochon, Y. J.,  
499 Shepherd, M. G., Solheim, B. H., Wang, D.-Y., and Ward, W. E.: The Wind Imaging  
500 Interferometer (WINDII) on the Upper Atmosphere Research Satellite: A 20 year perspective,  
501 *Rev. Geophys.*, 50, RG2007, doi:10.1029/2012RG000390, 2012.

502

503 Shepherd, M. G., Cho, Y.-M., Shepherd, G. G., Ward, W., and Drummond, J. R.:  
504 Mesospheric temperature and atomic oxygen response during the January 2009 major  
505 stratospheric warming, *J. Geophys. Res.*, 115, A07318, doi:10.1029/2009JA015172, 2010.

506

507 Shimazaki, T.: *Minor constituents in the middle atmosphere*, D. Reidel Publishing Company,  
508 Dordrecht, Holland, 1985.

509

510 Smith, A. K., Marsh, D. R., Russell III, J. M., Mlynczak, M. G., Martin-Torres, F. J., and  
511 Kyrölä, E.: Satellite observations of high nighttime ozone at the equatorial mesopause, *J.*  
512 *Geophys. Res.*, 113, D17312, doi:10.1029/2008JD010066, 2008.

513

514 Smith, A. K., Lopez-Puertas, M., Garcia-Comas, M., and Tukiainen, S.: SABER observations  
515 of mesospheric ozone during NH late winter 2002-2009, *Geophys. Res. Lett.*, 36, L23804,  
516 doi:10.1029/2009GL040942, 2009.

517

518 Smith, A. K., Marsh, D. R., Mlynczak, M. G., and Mast, J. C.: Temporal variation of atomic  
519 oxygen in the upper mesosphere from SABER, *J. Geophys. Res.*, 115, D18309,  
520 doi:10.1029/2009JD013434, 2010.

521



522 Sonnemann, G. R., Hartogh, P., Jarchow., C., Grygalashvyly, M., and Berger, U.: On the  
523 winter anomaly of the night-to-day ratio of ozone in the middle to upper mesosphere in  
524 middle to high latitudes, *Adv. Space Res.*, 40, 846-854, doi: 10.1016/j.asr.2007.01.039, 2007.

525

526 Sonnemann, G. R., Hartogh, P., Grygalashvyly, M., Li, S., and Berger, U.: The quasi 5-day  
527 signal in the mesospheric water vapor concentration in high latitudes in 2003 - a comparison  
528 between observations at ALOMAR and calculations, *J. Geophys. Res.*, 113, D04101, doi:  
529 10.1029/2007JD008875, 2008.

530

531 Sonnemann, G. R., Hartogh, P., Berger, U., and Grygalashvyly, M.: Hydroxyl layer: trend of  
532 number density and intra-annual variability, *Ann. Geophys.*, 33, 749–767, doi:10.5194/angeo-  
533 33-749-2015, 2015.

534

535 Sonnemann G., and Grygalashvyly, M.: The slow-down effect in the nighttime mesospheric  
536 chemistry of hydrogen radicals, *Adv. Space Res.*, 65, 2800-2807,  
537 doi:10.1016/j.asr.2020.03.025, 2020.

538

539 Takahashi, H., and Batista, P. P.: Simultaneous measurements of OH (9,4), (8,3), (7,2), 6,2),  
540 and (5,1) bands in the airglow, *J. Geophys. Res.*, 86, 5632–5642,  
541 doi:10.1029/JA086iA07p05632, 1981.

542

543 Takahashi, H., Clemesha, B. R., and Batista, P. P.: Predominant semi-annual oscillation of the  
544 upper mesospheric airglow intensities and temperatures in the equatorial region, *J. Atmos.*  
545 *Terr. Phys.*, 57(4), 407-414, doi:10.1016/0021-9169(94)E0006-9, 1995.

546



547 Takahashi, H., Batista, P. P., Buriti, R. A., Gobbi, D., Nakamura, T., Tsuda, T., and Fukao, S.:  
548 Response of the airglow OH emission, temperature and mesopause wind to the atmospheric  
549 wave propagation over Shigaraki, Japan, *Earth Planets Space*, 51, 863–875,  
550 doi:10.1186/BF03353245, 1999.

551

552 Taylor, M. J., Espy, P. J., Baker, D. J., Sica, R. J., Neal, P. C., and Pendleton, Jr. W. R.:  
553 Simultaneous intensity, temperature and imaging measurements of short period wave  
554 structure in the OH nightglow emission, *Planet. Space Sci.*, 39, 1171–1188, doi:  
555 10.1016/0032-0633(91)90169-B, 1991.

556

557 Varandas, A. J. C.: Reactive and non-reactive vibrational quenching in O + OH collisions,  
558 *Chem. Phys. Lett.*, 396, 182–190, doi:10.1016/j.cplett.2004.08.023, 2004.

559

560 Wachter, P., Schmidt, C., Wüst, S., and Bittner, M.: Spatial gravity wave characteristics  
561 obtained from multiple OH(3-1) airglow temperature time series, *J. Atmos. Sol. Terr. Phys.*,  
562 135, 192-201, doi: 10.1016/j.jastp.2015.11.008, 2015.

563

564 Walcek, C. J.: Minor flux adjustment near mixing ratio extremes for simplified yet highly  
565 accurate monotonic calculation of tracer advection, *J. Geophys. Res.*, 105, 9335-9348,  
566 doi:10.1029/1999JD901142, 2000.

567

568 Wiens, R. H., Moise, A., Brown, S., Sargoytchev, S., Peterson, R. N., Shepherd, G. G.,  
569 Lopez-Gonzalez, M. J., Lopez-Moreno J. J., and Rodrigo R.: SATI: A spectral airglow  
570 tempera-ture imager, *Adv. Space Res.* 1997, 19, 677–680, doi:10.1016/S0273-  
571 1177(97)00162-2, 1997.

572



573 Xu, J., Smith, A. K., Jiang, G., Gao, H., Wei, Y., Mlynchak, M. G., and Russell III, J. M.:  
574 Strong longitudinal variations in the OH nightglow, *Geophys. Res. Lett.*, 37, L21801,  
575 doi:10.1029/2010GL043972, 2010.

576

577 Xu, J., Gao, H., Smith, A. K., and Zhu, Y.: Using TIMED/SABER nightglow observations to  
578 investigate hydroxyl emission mechanisms in the mesopause region, *J. Geophys. Res.*, 117,  
579 D02301, doi:10.1029/2011JD016342, 2012.

580

581

582

583

584

585

586

587

588

589

590

591

592

593

594

595

596

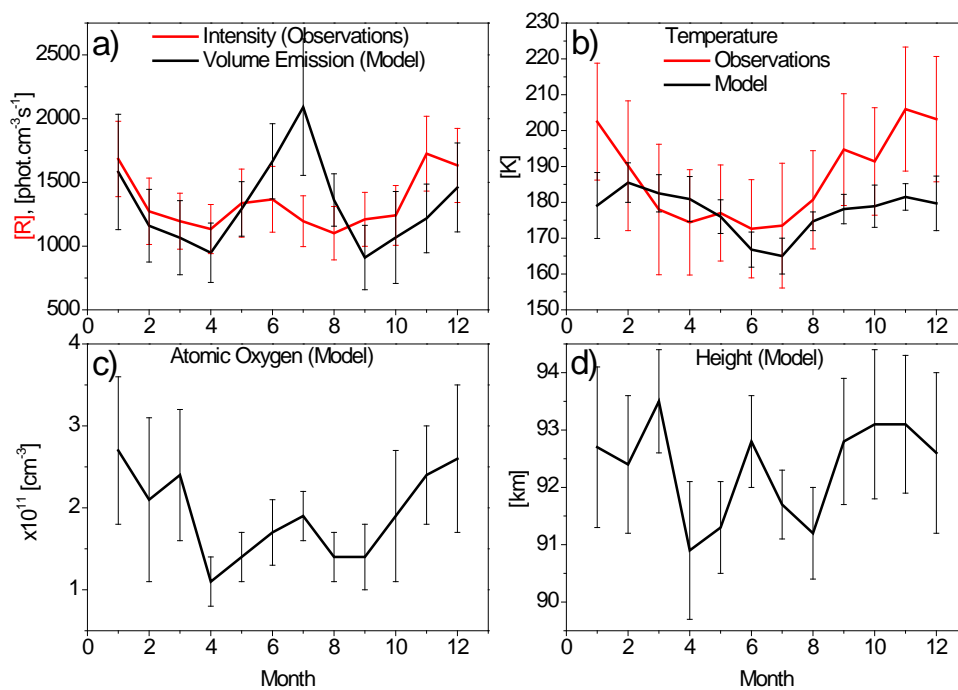
597

598



599 **Figures**

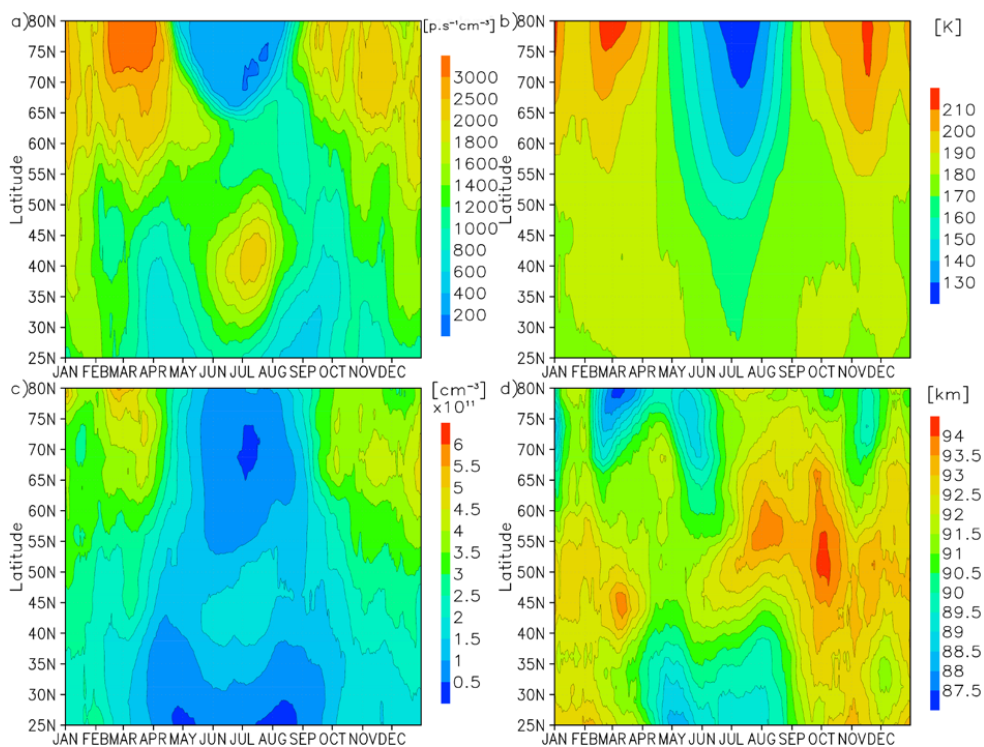
600 Figure 1. Observed at 43° N (black line) and modelled at 43.75° N (red line), annual  
601 variability of intensity and volume emission (a), temperature (b), atomic oxygen  
602 concentration (c), and height at the peak of the OH\*<sub>v=6</sub> layer.



603  
604  
605  
606  
607  
608  
609  
610  
611  
612  
613



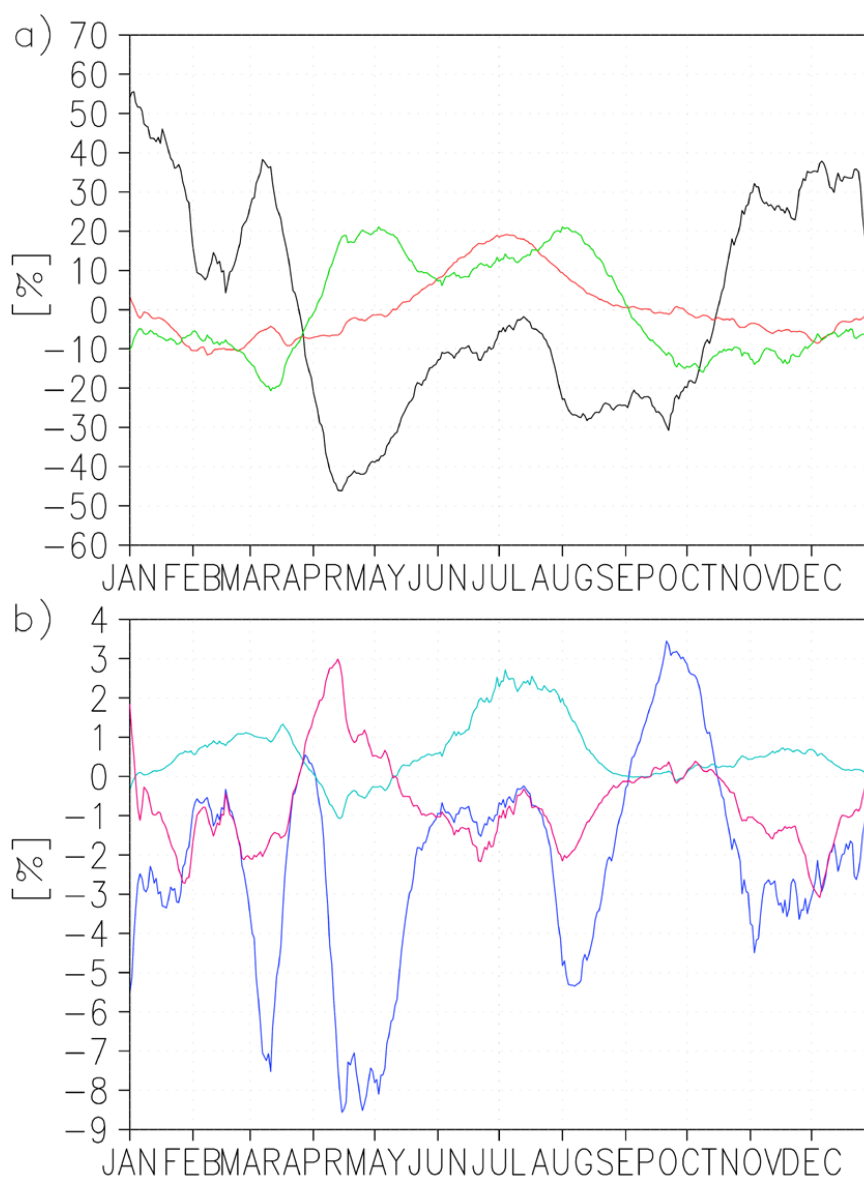
614 Figure 2. Nightly mean one-month sliding average volume emission (a), temperature (b),  
615 atomic oxygen at peak of  $\text{OH}^*_{v=6}$  (c), and height of peak of  $\text{OH}^*_{v=6}$ .



616  
617  
618  
619  
620  
621  
622  
623  
624  
625  
626  
627



628 Figure 3. a) relative to annual averaged variations of volume emission due to atomic oxygen  
629 (black line), temperature (red line), and height (green line) at 43.75° N, b) relative variations  
630 of volume emissions due to second momentum  $\frac{[O]M'}{[O]M}$  (blue line),  $\frac{T'M'}{TM}$  (cyan line), and  $\frac{[O]T'}{[O]T}$   
631 (magenta line) at 43.75° N.



632